Desmosomal COP9 regulates proteome degradation in arrhythmogenic right ventricular dysplasia/cardiomyopathy

Yan Liang,[1] Robert C. Lyon,[1] Jason Pellman,[1] William H. Bradford,[1] Stephan Lange,[1,2] Julius Bogomolovas,[1] Nancy D. Dalton,[1] Yusu Gu,[1] Marcus Bobar,[1] Mong-Hong Lee,[3] Tomoo Iwakuma,[4] Vishal Nigam,[5,6] Angeliki Asimaki,[7] Melvin Scheinman,[8] Kirk L. Peterson,[1] and Farah Sheikh[1]

[1]Department of Medicine, University of California San Diego, La Jolla, California, USA. [2]Institute of Medicine, Department of Molecular and Clinical Medicine and Wallenberg Centre for Molecular and Translational Medicine, University of Gothenburg, Gothenburg, Sweden. [3]Department of Molecular and Cellular Oncology, The University of Texas MD Anderson Cancer Center, Houston, Texas, USA. [4]Department of Cancer Biology, University of Kansas Medical Center, Kansas City, Kansas, USA. [5]Department of Pediatrics, University of California San Diego, La Jolla, California, USA. [6]Department of Pediatrics, Seattle Children's Research Institute and University of Washington, Seattle, Washington, USA. [7]Cardiology Clinical Academic Group, St. George's University of London, London, United Kingdom. [8]Department of Medicine, Cardiac Electrophysiology Section, University of California San Francisco, San Francisco, California, USA.

Dysregulated protein degradative pathways are increasingly recognized as mediators of human disease. This mechanism may have particular relevance to desmosomal proteins that play critical structural roles in both tissue architecture and cell-cell communication, as destabilization/breakdown of the desmosomal proteome is a hallmark of genetic-based desmosomal-targeted diseases, such as the cardiac disease arrhythmogenic right ventricular dysplasia/cardiomyopathy (ARVD/C). However, no information exists on whether there are resident proteins that regulate desmosomal proteome homeostasis. Here, we uncovered a cardiac constitutive photomorphogenesis 9 (COP9) desmosomal resident protein complex, composed of subunit 6 of the COP9 signalosome (CSN6), that enzymatically restricted neddylation and targeted desmosomal proteome degradation. CSN6 binding, localization, levels, and function were affected in hearts of classic mouse and human models of ARVD/C affected by desmosomal loss and mutations, respectively. Loss of desmosomal proteome degradation control due to junctional reduction/loss of CSN6 and human desmosomal mutations destabilizing junctional CSN6 were also sufficient to trigger ARVD/C in mice. We identified a desmosomal resident regulatory complex that restricted desmosomal proteome degradation and disease.

Introduction

The heart requires precise spatiotemporal control of cardiac protein turnover at distinct subcellular locations to maintain cardiac function, as dysregulated protein degradative pathways are increasingly recognized as mediators of human cardiac disease (1–3). These pathways may have special relevance to desmosomal proteins, which play critical structural roles in both tissue architecture and cell-cell communication, especially in organs that undergo constant mechanical stress, such as the heart (4, 5).

Five classic proteins that make up the cardiac desmosomal cell-cell junction protein complex, which we loosely term the desmosomal proteome, act to resist mechanical insult: desmoplakin (DSP), a central linker that tethers the tissue-specific desmosomal cadherins (desmoglein-2 [DSG2] and desmocollin-2 [DSC2]) to the intracellular intermediate filament cytoskeleton (desmin) via the intermediary armadillo proteins (plakoglobin [PKG] and plakophilin-2 [PKP2]) (4, 5). In the heart, the desmosomal complex acts alongside another mechanical junction, termed the fascia adherens junction (associated with the actin cytoskeleton) as well as electrical channels, known as gap junctions, to together synchronize muscle contraction (6). Genetic mutations in desmosomal genes resulting in the destabilization/breakdown of the desmosomal proteome are a central hallmark of all genetic-based desmosomal-targeted diseases (4, 7), including the cardiac disease arrhythmogenic right ventricular (RV) dysplasia/cardiomyopathy (ARVD/C) (8, 9). Protein degradation is a critical part of protein quality control and mainly performed by 2 pathways that include the ubiquitin-proteasome system and the autophagy-lysosome pathway (3). These pathways recycle damaged, misfolded, or unneeded proteins into free amino acids for future use (3). The cardiac cell-cell junction is thought to display signs of active protein degradation, as ubiquitin conjugates, autophagosomes, and markers of ubiquitin-mediated selective autophagy have been localized to these locations in both healthy and diseased cardiomyocytes (10–14). However, no information exists on whether there are resident proteins that regulate desmosomal (cell junction) proteome homeostasis.

Using an unbiased yeast-2-hybrid screen to search for desmosomal proteome regulators in the adult human heart in combina-

Conflict of interest: FS is a cofounder of Stelios Therapeutics Inc. (previously known as ARVC Therapeutics Inc.).

Submitted: March 9, 2020; **Accepted:** April 14, 2021; **Published:** June 1, 2021.
Reference information: *J Clin Invest*. 2021;131(11):e137689.
https://doi.org/10.1172/JCI137689.

tion with in silico molecular docking and in vivo genetic mouse and human heart tissue studies, we reveal protein degradation machinery that uniquely targets the cardiac desmosome to regulate desmosomal proteome longevity and function. We identify constitutive photomorphogenesis 9 signalosome subunit 6 (CSN6), a member of a pathway classically associated with protein quality control, as a resident desmosomal protein that endogenously restricts desmosome protein degradation to prevent the cardiac desmosomal targeted disease ARVD/C in mice and humans.

Results

Identification of CSN6 as a resident cardiac desmosomal protein. To identify proteins regulating cardiac desmosomal proteome homeostasis, we performed an unbiased yeast-2-hybrid screen using the human DSP N terminus (1–519 amino acids) as bait and an adult human heart cDNA library as prey. DSP was selected, as it is a central component in the desmosomal complex, and the N terminus was selected, as it is a major hub for interactions with desmosomal (armadillo) proteins (4) and hotspot for pathogenic ARVD/C mutations (15). We identified full-length CSN6 as an interacting partner of the DSP N terminus in the adult human heart. Forced yeast-2-hybrid assays validated the interaction between DSP N terminus and CSN6 (Figure 1A). In silico studies taking advantage of existing DSP and CSN6 crystal structures (16, 17) also showed that DSP and CSN6 structurally interfaced, as DSP N terminus (amino acids 179–625) could structurally complex with the signature Mpr1, Pad1 N-terminal (MPN) domain of CSN6 (Figure 1B). In the adult mouse heart, endogenous CSN6 coimmunoprecipitated with endogenous DSP as well as the desmosomal armadillo protein PKP2 (Figure 1C). Cardiac-specific *Csn6* inducible knockout (*Csn6*-iKO) heart extracts and IgG serum controls were used to demonstrate the specificity of CSN6 interactions to DSP and PKP2 (Figure 1C). CSN6 is also expressed in insoluble (junctional enriched) fractions and colocalized with DSP at the cardiac cell-cell junction in adult mouse hearts (Figure 1, D and E). Cardiac-specific *Dsp* knockout (*Dsp*-cKO) hearts also displayed a striking reduction in CSN6 protein levels (insoluble fraction) and localization at the cardiac cell-cell junction (Figure 1, D and E), highlighting CSN6 as an integral component of the cardiac desmosomal complex.

Cardiac CSN6 loss selectively accelerates desmosomal protein degradation in vivo. The COP9 signalosome (CSN), composed of 8 subunits (CSN1–CSN8), is evolutionarily conserved in eukaryotes and thought to have multifaceted roles in controlling ubiquitin-mediated protein degradation as well as acting as a signaling docking hub (18–20). However, the biological role of CSN6 in the heart has remained unclear. To determine the role of CSN6 in the postnatal heart in vivo, we generated 2 cardiac-specific *Csn6* knockout mice (Supplemental Figure 1, A–C; supplemental material available online with this article; https://doi.org/10.1172/JCI137689DS1) by using cardiac-specific a-myosin heavy chain–Cre (a-MHC–Cre) to create *Csn6*-cKO mice, and a cardiac-inducible a-MHC–MerCreMer mouse line to create *Csn6*-iKO mice, to assess its role in the early postnatal and adult heart, respectively (21, 22). Protein analyses revealed that CSN6 protein levels and junctional localization were lost in *Csn6* knockout hearts (Supplemental Figure 1, D–G). Given the direct protein interactions between CSN6 and DSP, we sought to assess the impact of CSN6 loss on the desmosomal proteome. CSN6 loss accelerated desmosomal protein complex destruction, as *Csn6* knockout hearts displayed selective loss of desmosomal protein levels when compared with those of controls (Figure 2). At early ages, mice harboring cardiac CSN6 loss resulted in primary loss of DSP as well as the gap junction (electrical) protein, connexin 43, in mice (Figure 2, A and C), which we have previously shown to be an early target of DSP loss (23). These early defects culminated into the total and specific destruction/loss of the desmosomal proteome at late ages in mice (Figure 2, B and D). We further highlight that global effects on the cardiomyocyte were not observed, as proteins residing in nondesmosomal (e.g., fascia adherens junction and costamere/plasma membrane proteins) structures within cardiomyocytes were not significantly affected in *Csn6* knockout hearts (Figure 2, B and D). RNA expression of desmosomal genes was also not affected in *Csn6* knockout hearts (Supplemental Figure 2), highlighting a posttranscriptional role for CSN6 within the desmosomal protein complex.

CSN6 loss renders the cardiomyocyte susceptible to hyperneddylation and targeted desmosomal protein degradation. Classic protein functions of CSNs are to enzymatically deneddylate and inactivate cullin RING E3 ubiquitin ligases (CURLs) to regulate ubiquitin-mediated protein degradation of targeted substrates (24). In vitro reconstitution assays refining the minimal CSN subunits required for deneddylation activity defined the CSN5-CSN6 heterodimer as sufficient and required to trigger deneddylation activity (17, 25); thus, we also sought to assess CSN5 localization in the adult mouse heart in the absence and presence of CSN6. We reveal that CSN5 is also localized to the cardiac cell junction in adult mouse hearts, similarly to CSN6 (Figure 3A). Furthermore, we show that its cell-junction localization was dependent on the presence of CSN6, as cardiac loss of CSN6 resulted in loss of CSN5 cell-cell junction localization and levels (Figure 3A), highlighting the presence of an active CSN subcomplex (consisting of CSN5 and CSN6) at the cardiac desmosome.

We further showed that CSN6 loss directly affected cullin neddylation–mediated control, as a select group of CURLs, namely cullin 1 and cullin 3 (migrating between 80 and 88 kDa), displayed a dramatic increase in their neddylated (higher molecular weight) forms in *Csn6*-iKO hearts (Figure 3, B and E). Immunofluorescence microscopy studies further revealed that CURLs that are directly affected (hyperneddylated) by CSN6 loss (e.g., cullin 3) are also localized to cell-cell junctions (Supplemental Figure 3). Consistent with these findings, we observed a striking increase in neddylation (at the 80–88 kDa range) as well as ubiquitination, a downstream target of neddylation in *Csn6*-iKO hearts (Figure 3, C, D, F, and G). Crosstalk between ubiquitination and selective autophagy-mediated pathways was also evident, as p62 levels were significantly upregulated in insoluble fractions of *Csn6*-iKO hearts (Figure 3, D and G). These observations are consistent with restricted effects of CSN6 loss at the cell-cell junction, as ultrastructural observations of hyperaccumulation of autophagic machinery were only observed at the cardiac cell-cell junction alongside destruction/loss of desmosomal structures (Figure 3H). Specifically, *Csn6*-iKO hearts revealed early defects in desmosomal integrity, which included the hyperaccumulation of autophagic vacuoles at the remnants of destroyed electron dense desmosomes

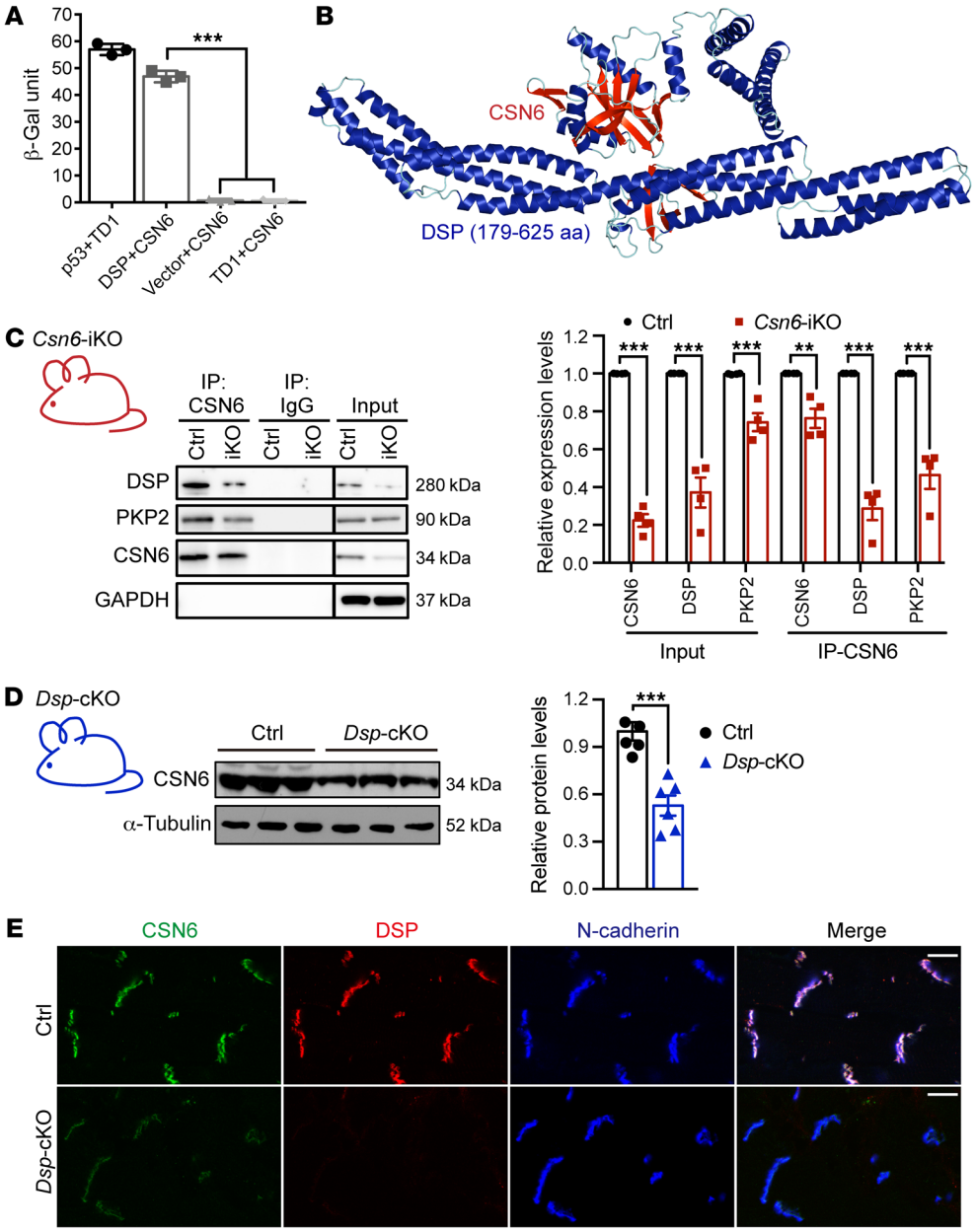

Figure 1. Identification of CSN6 as a cardiac desmosomal interacting protein. (**A**) Quantitative β-galactosidase (β-gal) activity assays from forced yeast-2-hybrid studies. p53 with TD1 served as positive control. Vector with CSN6 and TD1 with CSN6 served as negative controls. Data are represented as mean ± SEM; 1-way ANOVA with Tukey's multiple comparison test. ***$P < 0.001$. (**B**) In silico molecular docking of full-length CSN6 (red) and DSP N-terminus (amino acids 179–625, blue) was performed using ClusPro. Resulting models displayed a binding interface between the spectrin repeat encompassing R315 in DSP and the N-terminal MPN domain in CSN6, as these were identified as minimal binding sites in our biochemical analyses. (**C**) CSN6 was immunoprecipitated from control (Ctrl) and *Csn6*-iKO mouse heart extracts at 10 weeks of age and subjected to protein blot analyses and quantification for DSP, PKP2, and CSN6 protein levels, as indicated ($n = 4$ per group). IgG serum was used as a control. Input refers to total protein prior to coimmunoprecipitation assay. Relative expression of input proteins was normalized to the loading control GAPDH. Data are represented as mean ± SEM; 2-way ANOVA with Šidák's multiple comparison test. **$P < 0.01$; ***$P < 0.001$. Molecular weight standards are indicated. (**D**) Protein blot analysis and quantification of CSN6 protein levels in insoluble heart extracts from *Dsp*-cKO and control mice ($n = 6$ per group). The relative expression level of CSN6 was normalized to the loading control α-tubulin. Data are represented as mean ± SEM; Student's 2-tailed *t* test. ***$P < 0.001$. Molecular weight standards are indicated. (**E**) Immunofluorescence staining of DSP (red), CSN6 (green), and N-cadherin (blue) in *Dsp*-cKO and control mouse heart sections ($n = 3$ per group). Scale bar: 10 μm.

(e.g., often observed as wider/half desmosomal structures; Figure 3H). *Csn6*-iKO hearts also displayed hyperaccumulation of autophagic-like (multilayered) vesicles specifically at the cardiac cell junction (Figure 3H). The sufficiency of *Csn6* loss (Cre group) to target increased neddylation and ensuing ubiquitination was also observed in cardiomyocytes (Figure 4, A and D, and Supplemental Figure 4A). Using cycloheximide (CHX) chase assays, we show that CSN6 deficiency in cardiomyocytes results in a significant reduction in the half-life of key/core desmosomal proteins (which undergo more rapid degradation), demonstrating that protein degradation is specifically affected in *Csn6*-deficient cardiomyocytes (Figure 4, B and C). Restoration of CSN enzymatic function (via neddylation inhibitor MLN4924) and thus targeting of underlying deneddylation functions of CSN6 can also alleviate desmosomal protein loss caused by deletion of CSN6 (Figure 4D), highlighting desmosomal proteins as direct substrates of neddylation-mediated protein degradation.

Disruption of the CSN6-desmosomal complex and protein degradation pathways underlies ARVD/C in mice and humans. To determine the broad relevance of CSN6 pathways in desmosomal targeted diseases, we sought to assess CSN6 binding, localization, levels, and function in classic mouse and human models of ARVD/C affected by classic desmosomal loss/mutations. Hyperneddylation, hyperubiquitination, and an increase in p62 levels were observed in hearts of cardiac-specific *Dsp* knockout mice (Figure 5A and Supplemental Figure 4B) that harbored classic ARVD/C features (23) and a reduction in CSN6 localization at the cardiac cell-cell junction (Figure 1, D and E). Furthermore, ultrastructural analyses revealed hyperaccumulation of autophagic machinery

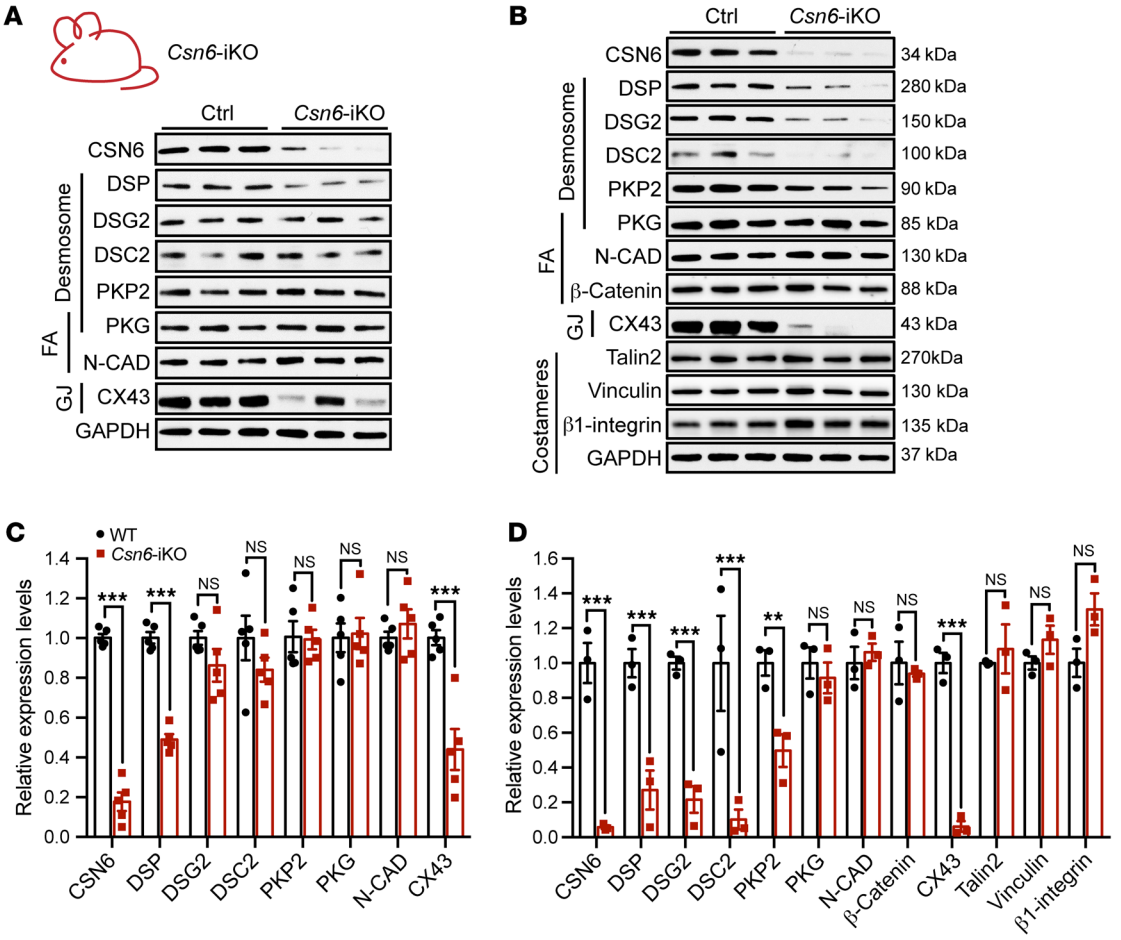

Figure 2. Cardiac CSN6 loss accelerated desmosomal protein dissolution in vivo. (**A** and **C**) Protein blot analyses (**A**) and quantification of protein expression levels (**C**) in total protein extracts from *Csn6*-iKO and control hearts at 2 weeks after tamoxifen injection (n = 5 per group). (**B** and **D**) Protein blot analyses (**B**) and quantification of protein expression levels (**D**) in total protein extracts from *Csn6*-iKO and control hearts at 6 weeks after tamoxifen injection (n = 3 per group). FA, fascia adherens; GJ, gap junction. The expression levels of proteins were normalized to the loading control GAPDH. Data are represented as mean ± SEM; 2-way ANOVA with Šidák's multiple comparison test. $^{**}P < 0.01$; $^{***}P < 0.001$.

at the cardiac cell-cell junction alongside destruction/loss of desmosomal structures (Figure 5B), similar to what was seen in *Csn6*-iKO hearts (Figure 3H). To determine whether CSN6 pathways are disrupted in human ARVD/C, we identified a patient with a clinical diagnosis of ARVD/C that carried a previously identified *DSP R315C* missense mutation (26) and pathogenic *PKP2 IVS10-1 G>C* splice site mutation (27, 28). This patient provided a genetic platform for assessing the importance of the CSN6-desmosomal interaction in human ARVD/C, as CSN6 can complex with both DSP and PKP2 (Figure 1C). The *DSP R315C* mutation was of interest, as it is an evolutionarily conserved amino acid within the DSP N terminus (Figure 5C), a region that could directly interact with CSN6 (Figure 1). In addition, the *DSP R315C* variant alone has been identified in patient populations harboring a sudden death syndrome (26), which parallels disease consequences of ARVD/C (sudden death). Analyses of the high-resolution crystal structure of human DSP (N terminal) plakin domain revealed that R315 is buried between the interface of 2 α-helices, where its charged sidechain stabilizes these adjacent α-helices (Figure 5D). Using in silico predictions, we showed that *DSP R315C* destabilizes the DSP plakin domain by breaking the electrostatic network of side chains that tether adjacent α-helices (Figure 5D), which in turn, we hypothesized lead to a disruption of DSP-CSN6 interaction. Forced yeast-2-hybrid assays revealed that the *DSP R315C* mutation abrogated the interaction between DSP and CSN6 (Figure 5E), reinforcing in silico predictions and the ability of this mutation to disrupt the DSP and CSN6 interaction. Consistent with these findings, CSN6 localization was lost at the cardiac cell junction in human ARVD/C heart harboring these same desmosomal mutations (Figure 5F). To further reinforce that destabilization of the desmosomal-CSN6 complex underlies human ARVD/C, we showcase findings from 5 autopsied ARVD/C hearts harboring classic desmosomal mutations (DSP and PKP2) that highlight reduced junctional localization of CSN6 as a recurrent molecular alteration observed in human ARVD/C hearts (Figure 6). N-cadherin (marker of fascia adherens junction) junctional localization was not affected in human ARVD/C hearts when compared with controls (Figure 6), further validating the specificity and relevance of junctional CSN6 dysregulation in human ARVD/C.

Loss of desmosomal proteome degradation control due to CSN6 loss is sufficient to trigger the desmosomal-targeted disease ARVD/C. Kaplan-Meier survival analyses revealed premature death of adult

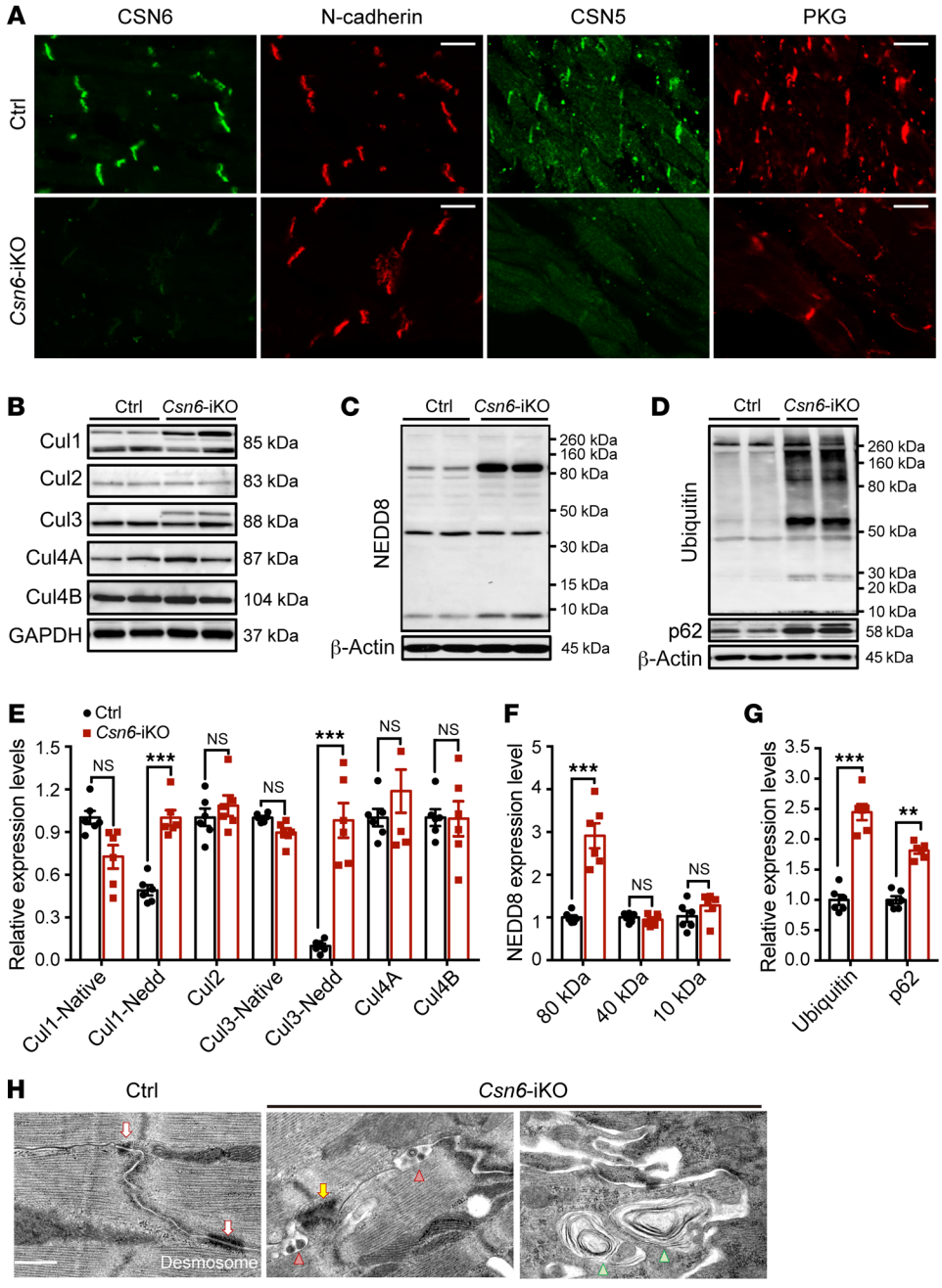

Figure 3. Neddylation-mediated protein degradation is affected by CSN6 loss. (**A**) Immunofluorescence staining of CSN subunits (CSN6 and CSN5, green) and cell-cell junctional markers (N-cadherin or PKG, red) in heart sections from *Csn6*-iKO and control mice at 2 weeks after tamoxifen injection (n = 3 per group). Scale bars: 20 μm. (**B**–**D**) Protein blot analyses of cullin E3 ligases (**B**), NEDD8 (**C**), ubiquitin, and p62 levels (**D**) in ventricular extracts from *Csn6*-iKO and control mice at 6 weeks after tamoxifen injection (n = 6 per group). (**E**–**G**) Quantification of protein expression levels in **B**–**D**, respectively. The expression levels of proteins were normalized to the loading control GAPDH or β-actin. Data are represented as mean ± SEM; 2-way ANOVA with Šidák's multiple comparison test. $^{**}P < 0.01$; $^{***}P < 0.001$. (**H**) Representative transmission electron micrographs from the RV of *Csn6*-iKO mice and littermate controls (n = 4 per group). White arrows denote desmosome. Yellow arrows denote disorganized desmosome. Red arrowheads denote autophagic vacuoles. Green arrowheads denote multimembraned "autophagic-like" vesicles. Scale bar: 500 nm.

Csn6 knockout mice (Figure 7, A and B). At late survival-curve time points, *Csn6* knockout mice displayed grossly enlarged and dilated cardiac chambers (Figure 7, C and D). Adult *Csn6* knockout mouse hearts also displayed extensive ventricular fibrosis and pronounced lipid deposition that was restricted to the myocardium and "triangle of dysplasia" (Figure 7, E and F, and Supplemental Figure 5, A and B), reminiscent of pathological fibrofatty infiltration found in human ARVD/C hearts (29). We further revealed biventricular dilatation, dysfunction, and failure in adult *Csn6* knockout mouse hearts (Figure 7, G and H, and Supplemental Figure 5C), which is reminiscent of a biventricular form of human ARVD/C and is in accordance with the recent adoption of the term arrhythmogenic cardiomyopathy to reference this class of diseases (30). At early survival-curve time points, adult *Csn6*-iKO hearts displayed preserved cardiac dimensions and function (Supplemental Figure 5D). Instead, electrocardiography tracings revealed the presence of frequent premature ectopic beats/arrhythmias as well as ventricular depolarization delay in *Csn6*-iKO hearts (Figure 7, I and J, and Supplemental Figure 5E), reminiscent of early electrical defects found in human ARVD/C patients (8, 31). These data demonstrate the sufficiency of cardiac CSN6 loss to trigger classic electrical and structural features associated with human ARVD/C.

Human desmosomal mutations destabilizing CSN6 are sufficient to trigger the desmosomal targeted disease ARVD/C. To precisely validate and extrapolate how desmosomal (compound) mutations found in the human ARVD/C patient affect CSN6 interactions and functions in an independent adult heart setting, we generated compound heterozygous mice harboring the same human

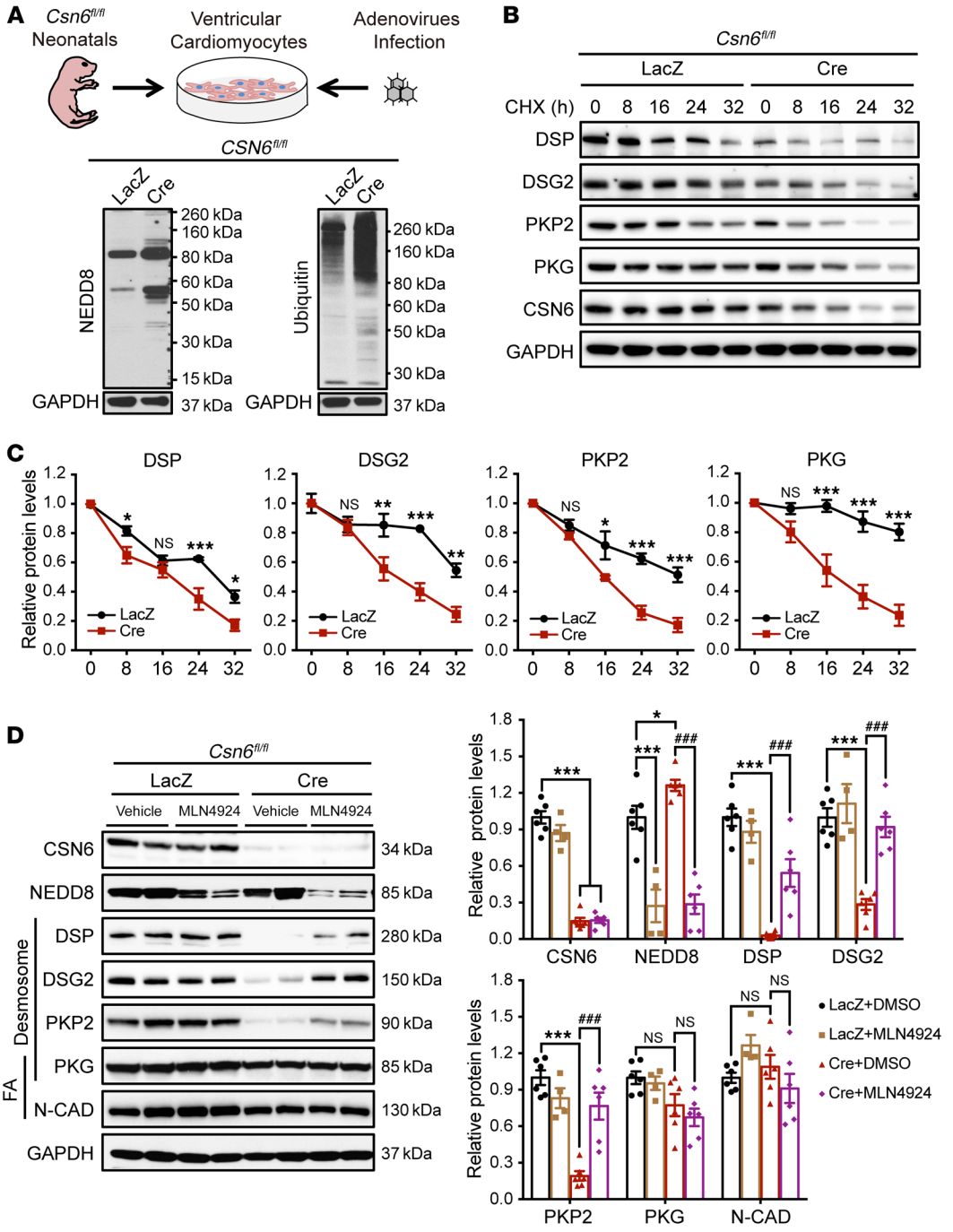

Figure 4. CSN6-mediated protein degradation pathway targets desmosomal proteome degradation. (**A**) Schematic depiction of neonatal CSN6 floxed mice, which were used for neonatal ventricular cardiomyocyte studies(top). Protein blot analyses of NEDD8 and ubiquitin levels in *Csn6*-deficient (Cre, MOI 100) and control (lacZ, MOI 100) ventricular cardiomyocytes (bottom). Experiments were repeated independently 3 times (2 wells per condition) with similar results. (**B** and **C**) Representative protein blots (**B**) and quantification analyses (**C**) of desmosomal proteins in *Csn6*-deficient (Cre, MOI 100) and control (lacZ, MOI 100) ventricular cardiomyocytes. After 48-hour infection, cardiomyocytes were treated with CHX (10 μg/mL) for 0, 8, 16, 24, and 32 hours. Expression levels of proteins were normalized to the loading control GAPDH. Data are represented as mean ± SEM; 2-way ANOVA with Šidák's multiple comparison test. $^{*}P < 0.05$; $^{**}P < 0.01$; $^{***}P < 0.001$. (**D**) Protein blot analyses and quantification of protein expression levels of cell-cell junction proteins and NEDD8 levels in *Csn6*-deficient (Cre, MOI 100) and control (lacZ, MOI 100) ventricular cardiomyocytes in the presence of vehicle or MLN4924 treatment. Expression levels of proteins were normalized to the loading control GAPDH. Data are represented as mean ± SEM; 2-way ANOVA with Šidák's multiple comparison test. $^{*}P < 0.05$; $^{***}P < 0.001$, when compared with the control cardiomyocytes treated with DMSO (LacZ+DMSO). $^{###}P < 0.001$, when compared with the *Csn6*-deficient cardiomyocytes treated with DMSO (Cre+DMSO). Experiments were repeated independently 3 times (2 wells per condition) with similar results.

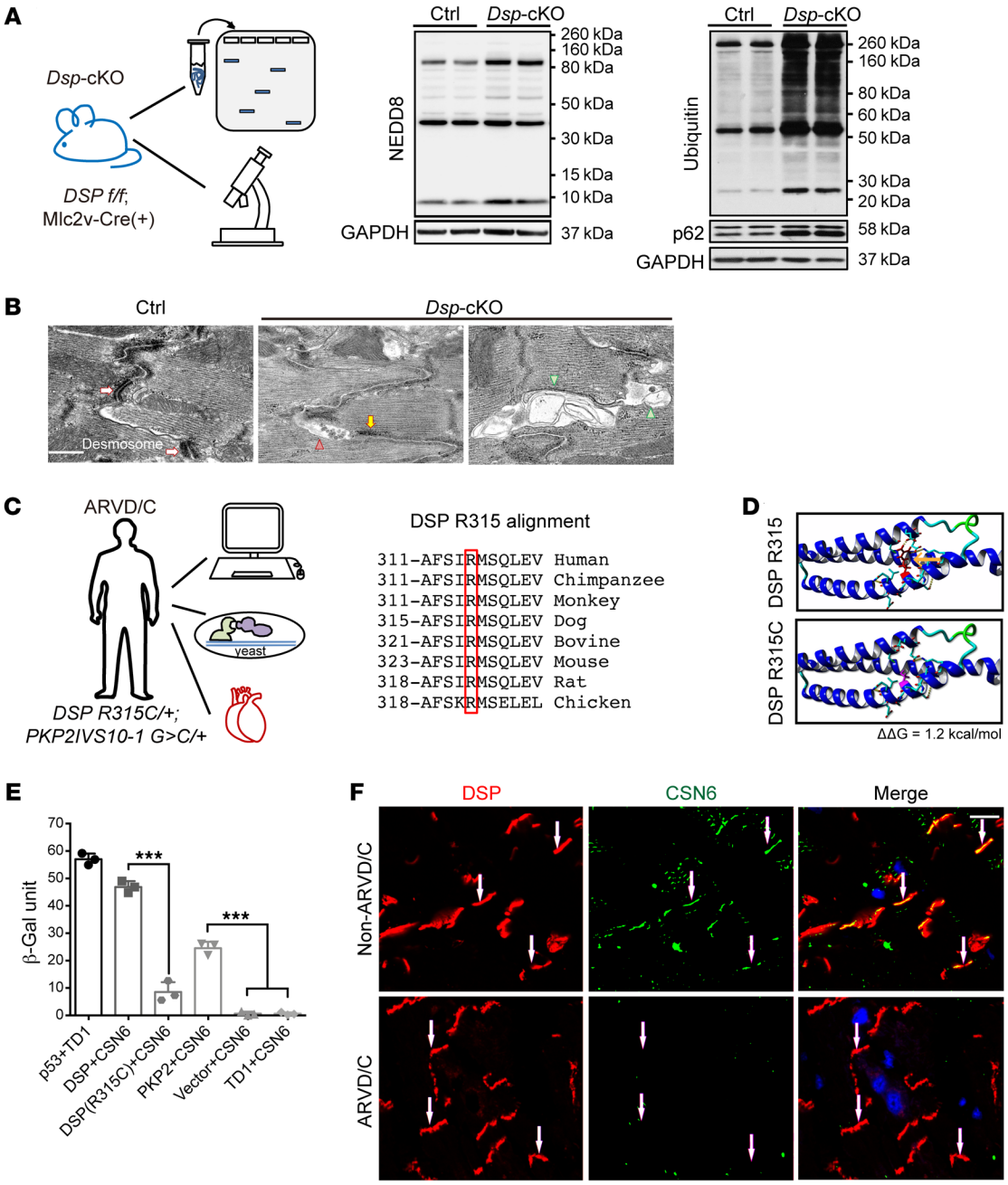

Figure 5. Disruption of the CSN6-desmosomal complex and protein degradation pathways underlies ARVD/C in mice and man. (**A**) Schematic depiction of *Dsp*-cKO mice, which were utilized to perform cardiac protein and transmission electron microscopy analyses (left). Protein blot analysis of NEDD8, ubiquitin, and p62 levels in ventricular extracts from *Dsp*-cKO and control mice at 8 weeks of age (n = 5–6 per group) (right). (**B**) Representative transmission electron micrographs from the RV of *Dsp*-cKO and littermate control (n = 4 per group). White arrows denote desmosome. Yellow arrows denote disorganized desmosome. Red arrowheads denote autophagic vacuoles. Green arrowheads denote multimembraned "autophagic-like" vesicles. Scale bar: 500 nm. (**C**) Schematic representation of assays used to interrogate the role of *DSP R315C* mutation identified from an ARVD/C patient (left). DSP R315 region sequence alignment across vertebrate species. Red square denotes R315 (right). (**D**) In silico molecular docking studies of DSP R315 (top) and R315C mutation (bottom). ΔΔG (change from R315 to R315C) is predicted with FoldX. ΔΔG > 0 = destabilizing and ΔΔG < 0= stabilizing. (**E**) β-Galactosidase activity from forced yeast-2-hybrid studies. p53 with TD1 served as a positive control. Vector with CSN6 and TD1 with CSN6 served as negative controls. Data are represented as mean ± SEM; 1-way ANOVA with Tukey's multiple comparison test. ***P < 0.001. p53+TD1, DSP+CSN6, vector+CSN6, and TD1+CSN6 data in Figure 5E are also presented in Figure 1A. (**F**) Immunofluorescence staining of DSP (red) and CSN6 (green) in heart biopsies from an ARVD/C patient (harboring *DSP R315C* and *PKP2 IVS10-1 G>C* mutations) and non-ARVC control. White arrows denote cell-cell junction. Scale bar: 10 μm.

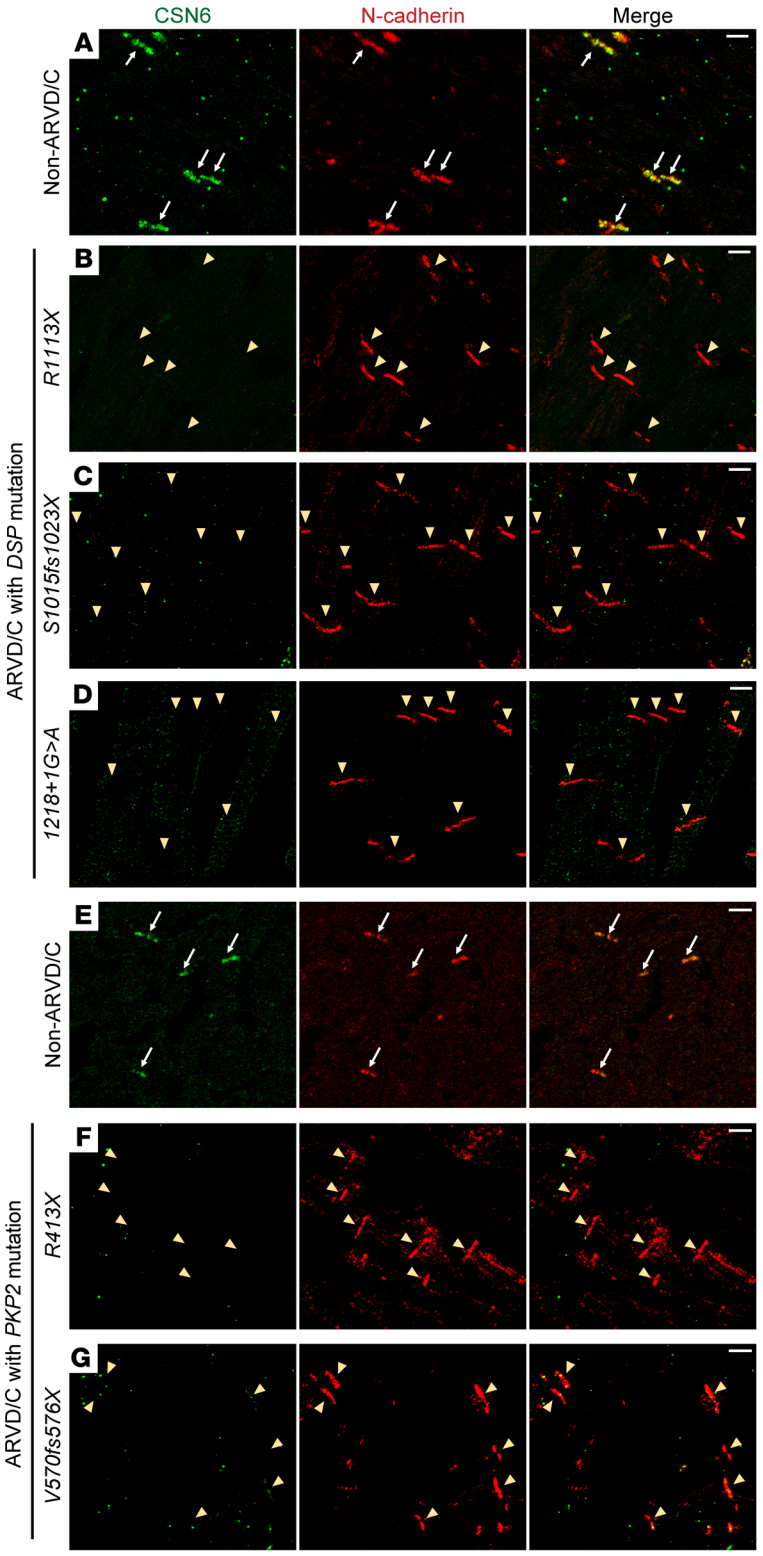

Figure 6. Human desmosomal mutations associated with ARVD/C affect CSN6 localization. (**A**–**G**) Immunofluorescence staining of N-cadherin (red) and CSN6 (green) in ARVD/C heart autopsy tissues harboring *DSP* or *PKP2* mutation and non-ARVD/C controls. White arrows denote the cell-cell junctions, which express both CSN6 and N-cadherin. Yellow arrowheads denote the cell-cell junctions, which only express N-cadherin. Scale bars: 10 μm.

desmosomal mutations (Double Het, *Dsp R315C/+*; *Pkp2 IVS10-1 G>C/+*; Supplemental Figure 6, A–F). GST pull-down assays exploiting GST-CSN6 and Double Het heart extracts (for native DSP) highlighted the significant reduction of DSP binding to CSN6 in Double Het hearts (Figure 8, A and B). These molecular alterations led to a significant reduction in junctional CSN6 and desmosomal protein levels, including DSP and PKP2, as well as downstream targets, such as connexin43 in RV cell-cell junction extracts from Double Het hearts when compared with controls (Figure 8, C and E). Proteins found in nondesmosomal compartments (e.g., N-cadherin, marks fascia adherens junction) were not significantly affected in Double Het mice (Figure 8, C and E), highlighting specificity of junctional targets affected by CSN6 loss. An impact on protein degradation pathways consistent with loss of CSN6 function was observed in Double Het hearts, as a significant increase in neddylation (at the 80-88 kDa range) was observed when these were compared with controls (Figure 8, D and E). Using CHX chase assays, we also showed a significant and progressive reduction in the half-life of key desmosomal proteins (triggering their rapid degradation) in neonatal Double Het cardiomyocytes (Supplemental Figure 6, G and H), highlighting an early (neonatal) and specific impact of reduced junctional localization of CSN6 on desmosomal protein degradation in Double Het hearts. Adult Double Het mice exhibited classic features associated with ARVD/C, which also recapitulated disease features found in *Csn6*-deficient mice. These included primary RV defects (dilatation) (Figure 8F), in the absence of changes in left ventricular (LV) dimensions and function in Double Het hearts at an early age (Supplemental Figure 6I). Electrocardiography tracings also revealed the presence of frequent cardiac premature ectopic beats/arrhythmias in Double Het mice (Figure 8G). Electrical and functional deficits could be exacerbated with age in Double Het hearts, as they exhibited evidence of recurrent baseline arrhythmias associated with ventricular depolarization delay (QRS prolongation) as well as cardiac enlargement associated with LV functional deficits (Figure 8, H–K). Since we predicted that the *Dsp R315C* was sufficient on its own to destabilize interactions to CSN6, we also characterized single *Dsp R315C* homozygous mutant mice (*Dsp* Hom). GST pull-down assays exploiting GST-CSN6 and *Dsp* Hom heart extracts (for native DSP) highlighted that these hearts now exhibited a complete abrogation in cardiac DSP binding to CSN6 (Supplemental Figure 7A). We show that deficits in these pathways were sufficient to trigger baseline electrical deficits (ventricular depolarization delay) and cardiac functional insufficiencies (reduced percentage of fractional shortening [FS]) associated with ARVD/C in *Dsp* Hom mice (Supplemental Figure 7, B and D). Since exercise/catecholamines are known to exacerbate arrhythmias in ARVD/C (32, 33), we assessed arrhythmias in *Dsp* Hom mice in the context of isoproterenol (catecholamine) stress. We show that

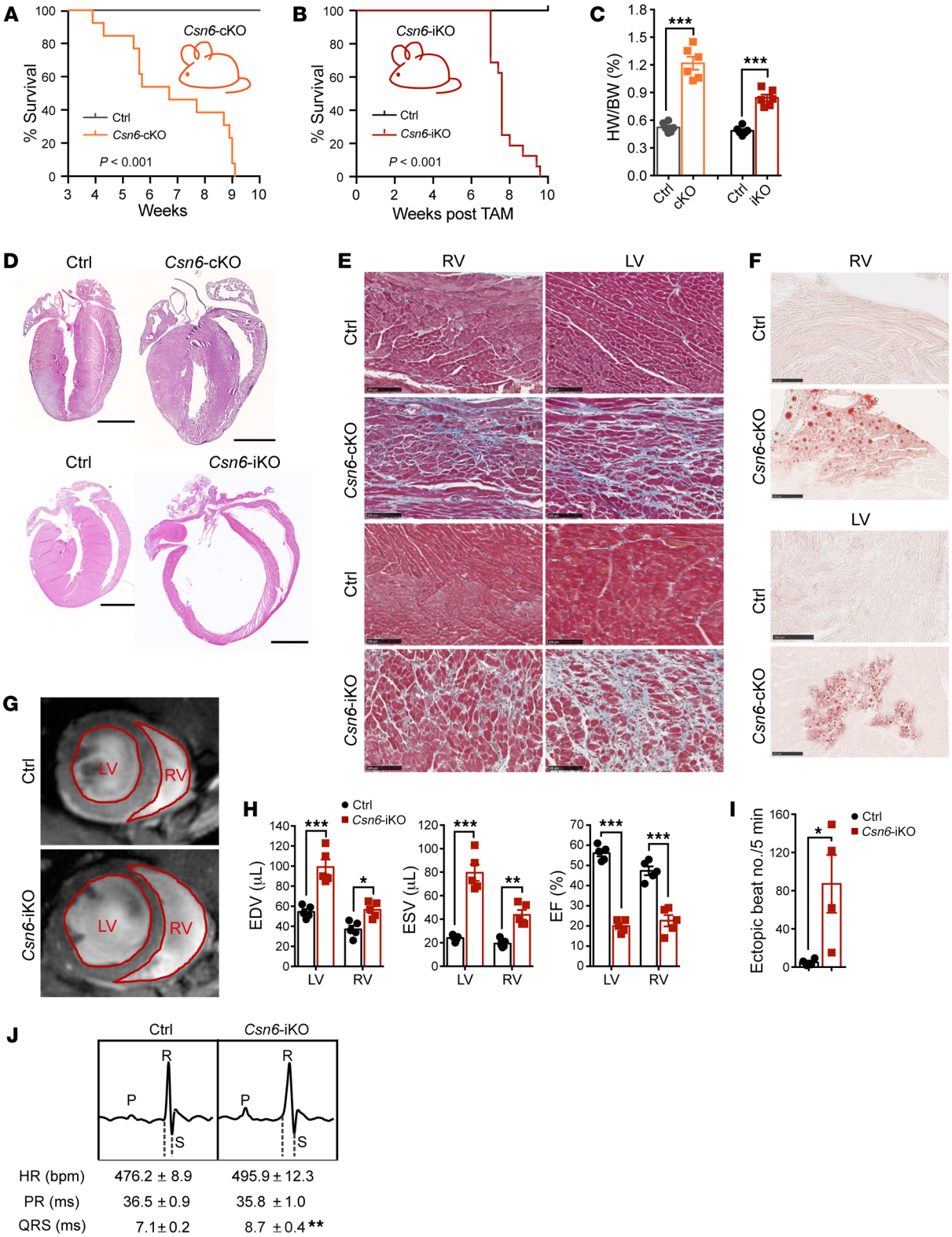
A
% Survival
Csn6-cKO
Ctrl
Csn6-cKO
P < 0.001
Weeks
B
% Survival
Csn6-iKO
Ctrl
Csn6-iKO
P < 0.001
Weeks post TAM
C
HW/BW (%)
***
***
Ctrl
cKO
Ctrl
iKO
D
Ctrl
Csn6-cKO
Ctrl
Csn6-iKO
E
RV
LV
Ctrl
Csn6-cKO
Ctrl
Csn6-iKO
F
RV
Ctrl
Csn6-cKO
LV
Ctrl
Csn6-cKO
G
Ctrl
Csn6-iKO
LV
RV
LV
RV
H
Ctrl
Csn6-iKO
EDV (μL)
ESV (μL)
EF (%)
LV
RV
I
Ectopic beat no./5 min
Ctrl
Csn6-iKO
J
Ctrl
Csn6-iKO
R
P
S
HR (bpm) 476.2 ± 8.9 495.9 ± 12.3
PR (ms) 36.5 ± 0.9 35.8 ± 1.0
QRS (ms) 7.1 ± 0.2 8.7 ± 0.4 **

Figure 7. Cardiac-specific loss of CSN6 in mice results in sudden death and recapitulates key disease features of ARVD/C. (**A** and **B**) Kaplan-Meier survival curve analysis of *Csn6*-cKO and control (**A**, *n* = 13) as well as *Csn6*-iKO and control (**B**, *n* = 16) mice after tamoxifen injection (log-rank test). (**C**) Heart weight to body weight ratios (HW/BW) from control and *Csn6*-deficient mice (*n* = 6 per group). Data are represented as mean ± SEM; 2-way ANOVA with Šidák's multiple comparison test. ***$P < 0.001$. (**D**) Representative whole-heart sections from *Csn6*-deficient and control mice at 6 weeks of age or after tamoxifen injection (*n* = 4 per group). Sections were stained for nuclei and cytoplasm with hematoxylin and eosin, respectively. Scale bars: 2 mm. (**E**) Representative Masson's trichrome–stained cardiac sections from *Csn6*-deficient and control mice at 6 weeks of age or after tamoxifen injection (*n* = 4 per group). Scale bars: 100 μm. (**F**) Representative oil red O–stained cardiac sections from *Csn6*-cKO and control mice at 6 weeks of age (*n* = 4 per group). Scale bars: 100 μm. (**G**) Representative MRI images (short axis) from control and *Csn6*-iKO hearts at 6 weeks after tamoxifen injection (*n* = 5 per group). (**H**) MRI analyses of left and RV ejection fractions (EF), EDV, and ESV in control and *Csn6*-iKO hearts at 6 weeks after tamoxifen injection. Data are represented as mean ± SEM; 2-way ANOVA with Šidák's multiple comparison test. **$P < 0.01$; ***$P < 0.001$. (**I**) Quantification of number of ectopic beats in *Csn6*-iKO and control mice (*n* = 4 per group) at 2 weeks after tamoxifen injection. Data are represented as mean ± SEM; Student's 2-tailed *t* test. *$P < 0.05$. (**J**) Representative surface ECG tracings in *Csn6*-iKO and control mice at 2 weeks after tamoxifen injection (*n* = 10 per group). Quantification of heart rate (HR), PR, and QRS intervals from ECG tracings was performed. Data from 100 ECG tracings per mouse were averaged for analysis. Data are represented as mean ± SEM; Student's 2-tailed *t* test. **$P < 0.01$. QRS duration is indicated by the dotted line.

Dsp Hom mice exhibited a significant increase in catecholamine-induced arrhythmias when compared with controls (Supplemental Figure 7C), further highlighting electrical deficits associated with ARVD/C. These data together highlight the importance of the DSP-CSN6 interaction (and their alterations in the context of classic human desmosomal mutations) as a trigger to the cardiac-remodeling response associated with human ARVD/C in mice.

Discussion

We provide evidence for the presence of an enzymatically active CSN subcomplex (containing core subunits CSN5 and CSN6) at the cardiac desmosome that targets its degradation. We show that CSN6 is an integral component of the cardiac desmosomal complex tethered by a direct interaction with the N terminus of DSP. Taking advantage of DSP and CSN6 crystal structures (16, 17), our studies revealed the minimal DSP-CSN6 binding interface, which occurs between the spectrin repeats in the N terminus of DSP and the MPN domain of CSN6. Deneddylation activity requires the MPN domain of CSN, as evidenced by deletion studies in which a CSN6 fragment of the MPN domain resulted in a 100-fold decrease in deneddylation activity (17). Further refinement of the minimal CSN subunits required for deneddylation activity has identified the sufficiency and requirement of the CSN5-CSN6 heterodimer to trigger deneddylation activity (17, 25). CSN5 is the only COP9 complex subunit that harbors enzymatic activity, as a protease as its MPN domain contains an embedded JAB1 MPN domain metalloenzyme (JAMM) motif, which contains the required catalytic center to deneddylate substrates (19, 34). We show that CSN5 is colocalized to cell junctions in the adult mouse heart and that its cell junction localization was dependent on the presence of CSN6, highlighting the presence of a minimal CSN subcomplex. In vitro studies have revealed that the CSN5-CSN6 heterodimer is sufficient to deneddylate and facilitate CURL function (25), suggesting functional sufficiency of this minimal CSN subcomplex to enzymatically target substrates. Our studies highlight that CSN5-CSN6 likely heterodimerizes at desmosomal junctions, but CSN5 may exclusively function to deneddylate CURLs and target desmosomal proteins for degradation. Future studies focused on disrupting the CSN5/6 heterodimer will be required to determine whether CSN5 is also required for desmosomal substrate recognition.

What we believe is the novelty of our studies lies in the identification of a desmosomal substrate recognition and protein turnover system imprinted within the desmosomal resident complex in the heart. The molecular architecture of the protein-protein interactions that define the desmosomal resident complex includes desmosomal structural proteins DSP (spectrin domain) and PKP2, which have a native affinity to the MPN domain of the core CSN member, CSN6, and thus are recognized by neddylation-based protein degradation machinery. This concept is validated by our studies that show CSN6 interactions with desmosomal proteins DSP and PKP2 in the adult mouse heart as well as the sufficiency of human desmosomal mutations in DSP and PKP2 to elicit reduction/abrogation of junctional localization of CSN6 in the adult mouse and human heart. CSN6's known interactions (heterodimerization) with CSN5 act to form a subcomplex at the desmosomal cell-cell junction to deneddylate/inactivate specific CURLs (e.g., cullin 3) to prevent desmosomal protein ubiquitination and degradation. This concept is validated in *Csn6* knockout hearts, as they exhibit hyperneddylated forms of select CURLs (cullins 1 and 3, which migrate at the 80–88 kDa range), further revealing CSN6-dependent cullins. We also show that CURLs, such as cullin-3, are localized to cell-cell junctions, highlighting an epicenter in the cardiomyocyte that contains "enzymatically" functional COP9 machinery for deneddylation activity. We speculate that CSN5's enriched expression at the cell-cell junction may also be the reason that global effects of CSN6 loss are not observed in other compartments of the cardiomyocyte despite CSN6 residing in areas outside of the desmosome. MLN4924 (neddylation inhibitor) studies highlight the essential role of CSN6 in deneddylation functions, as MLN4924 could alleviate the desmosomal protein loss caused by deletion/loss of CSN6. The CSN complex has been hypothesized to form a "holocomplex" containing all 8 CSNs as well as smaller subcomplexes with a subset of CSNs such as CSN1/2/3/8 and CSN4/5/6/7 (35, 36). Our studies highlight enrichment of a subset of CSN subunits to the cell-cell junction, as previous studies in the field utilizing cardiac-specific *Csn8* knockout mice highlight the absence of CSN8 localization to the cell-cell junction (20, 37). Future studies focused on dissecting whether other CSN members associate or functionally affect the desmosomal resident complex will be required to identify the CSN6 subcomplex members and dynamics restraining desmosomal protein degradation in cardiomyocytes.

Our studies highlight that junctional reduction/loss of CSN6 is a central feature that drives derailed protein degradation and ARVD/C (diagnostic predictor of severity) in mice and humans. We show, using human myocardial tissue, that reduced junc-

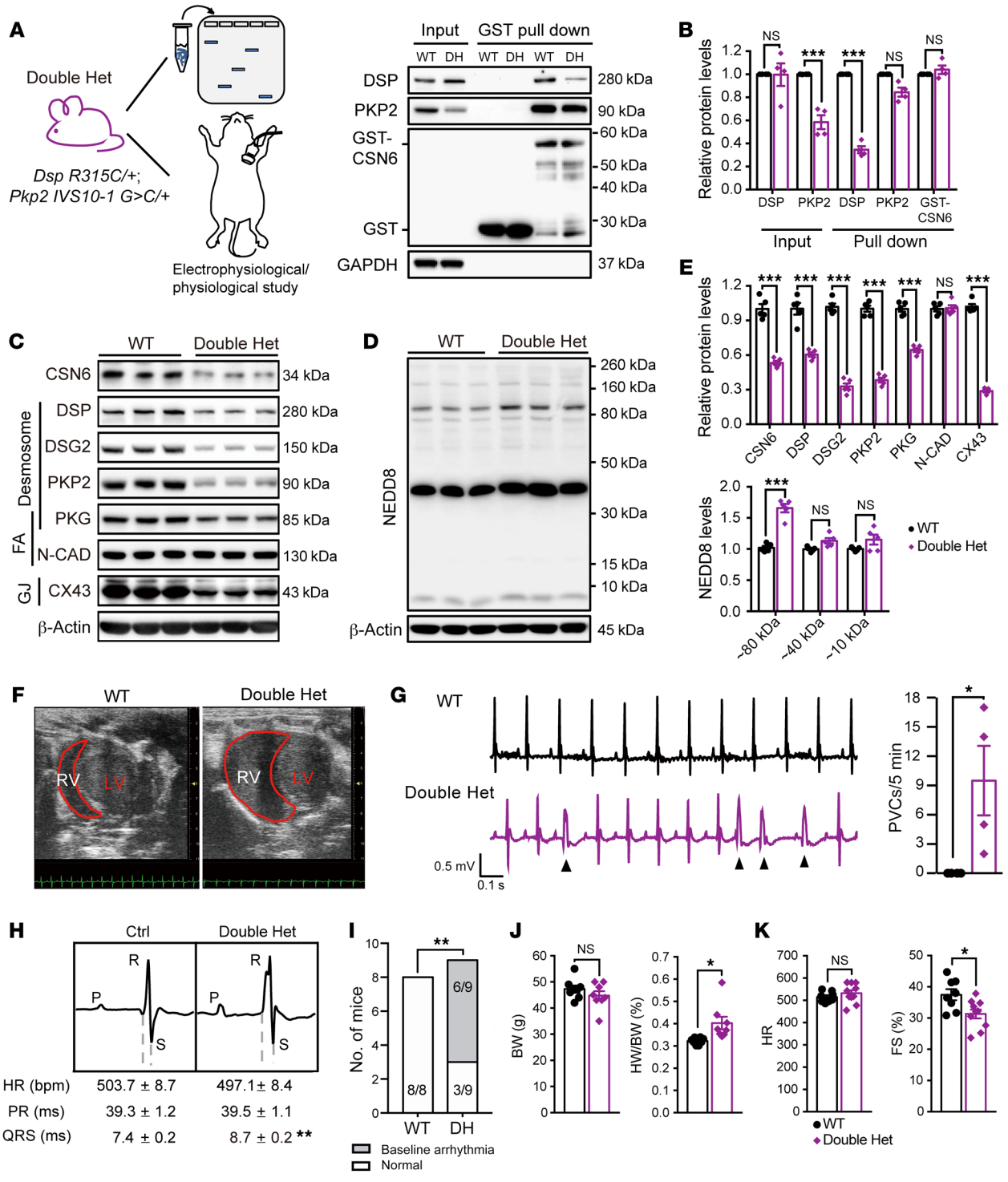

Figure 8. Human desmosomal mutations that destabilize CSN6 are sufficient to disrupt CSN6 expression and neddylation and trigger ARVD/C features in mice. (**A** and **B**) Schemata of assays used to interrogate the double heterozygous Dsp R315C/+; Pkp2 IVS10-1 G>C/+ mutation in mice (left). Protein analyses (**A**) and quantification (**B**) following GST pulldown assay. GST and GST-CSN6 protein were incubated with the heart extracts from WT and Double Het mice at 4 months of age (n = 4 per group). The expression levels of input proteins were normalized to GAPDH. (**C**–**E**) Protein analysis of cardiac cell-cell junction (**C**), NEDD8 expression levels (**D**), and quantification (**E**) in RV insoluble extracts from Double Het and WT mice at 4 months of age (n = 5 per group). The expression levels of proteins were normalized to β-actin. (**F**) Representative apical 4 chamber views from echocardiography (n = 6 per group) at 4 months of age. (**G**) Representative surface ECG tracing and quantification of premature ventricular contractions (PVCs) (n = 4 per group) at 4 months of age. (**H**) Representative surface ECG tracings in Double Het and WT mice at 1 year of age (n = 8–9 per group). Data from 100 ECG tracings per mouse were averaged for analysis of heart rate, PR, and QRS intervals. (**I**) Quantification of number of Double Het and WT mice that displayed baseline arrhythmia during ECG recording at 1 year of age (n = 8–9 per group). χ^2 test. (**J**) Body weight and heart weight to body weight ratios from Double Het and WT mice at 1 year of age (n = 8 per group). (**K**) Echocardiographic M-mode analysis of LV dimensions and function in Double Het and WT mice at 1 year of age (n = 8–10 per group). Data are represented as mean ± SEM; 2-way ANOVA with Šidák's multiple comparison test (**B** and **E**); Student's 2-tailed t test (**G**, **H**, **J**, and **K**). *P < 0.05; **P < 0.01; ***P < 0.001.

tional localization of CSN6 is a molecular hallmark of ARVD/C associated with classic desmosomal mutations. We further show that cardiac *Csn6*-KO mice could recapitulate all classic disease features of ARVD/C. Central to these features is the loss of neddylation-mediated degradation control in *Csn6*-KO hearts, which triggered hyperaccumulation of ubiquitin and selective autophagy protein degradation machinery at the cardiac desmosome to target its structural destruction. The interplay between neddylation and ubiquitination in *Csn6*-KO hearts further highlights the sensitivity of the cardiomyocyte to stress associated with dysregulation of protein turnover pathways. Previous studies in cardiomyocytes showcase that disturbing the balance of COP9 function (by removing the complex subunit CSN8) can in fact lead to proteotoxicity (by overwhelming the ubiquitin proteasome system), which resulted in increased ubiquitination (20, 37). Our studies focused on deleting *Csn6* highlight similar consequences whereby cardiomyocyte CSN6 deficiency results in increased neddylation (increased CURL activity) in cell-cell junction fractions, leading to increases in ubiquitylation of substrate proteins that overwhelm the proteasome and autophagy systems (e.g., accumulation of autophagic structures) at this location, thus resulting in increased accumulation of ubiquitination. These results validate prior findings, but give, in addition, more mechanistic insights into the interplay between neddylation and ubiquitination in cardiomyocytes. Interestingly, similar ultrastructural findings of accumulated protein degradation machinery at cell junctions have been reported in independent ARVD/C settings in mice and humans (38, 39). Furthermore, we show that hearts from a classic ARVD/C mouse model (*Dsp*-cKO) displayed reduced junctional localization of CSN6 and similar protein degradation defects, consistent with loss of CSN6 function. Finally, we show the sufficiency of mice harboring human desmosomal mutations (Double Het, *Dsp* Hom) to destabilize junctional-associated CSN6 and trigger protein degradation defects (including triggering rapid desmosomal protein degradation) and cardiac disease (ARVD/C) features consistent with loss of CSN6 function. Interestingly, the rapid degradation of desmosomal proteins (reduced half-life of desmosomal proteins) observed in neonatal Double Het cardiomyocytes further highlights the early disease consequences stemming from junctional reduction/loss of CSN6 in ARVD/C. Despite these findings, we cannot exclude the possibility that primary effects of desmosomal mutations contribute to ARVD/C disease causality in Double Het and *Dsp* Hom mice as opposed to CSN6 alone, given the complex nature of protein-protein interactions in the desmosomal resident complex and signalosome. Future studies focused on dissecting the impact of CSN6 functional restoration in Double Het and *Dsp* Hom mice will be required to determine whether ARVC disease causality is solely attributed to CSN6 loss in these models.

These studies set the stage to potentially reclassify desmosomal diseases, such as ARVD/C, as diseases of desmosomal protein degradation as well as provide mechanistic insights on new targets for intervention (deneddylation) for ARVD/C, which can be exploited to restore the whole desmosomal proteome in a setting where desmosomal variants can no longer bind proteins that are required to maintain their structure (e.g., CSN6). We also identify compartmentalized functions for subunits of a classically large protein degradation signalosome complex, like COP9, as well as the structural interface (spectrin-MPN domain interaction) of how CSNs may target select substrates. Studies in desmosomal mutant mice (Double Het; *Dsp* Hom) further reveal that the heart dysfunction and arrhythmias associated with CSN6 reduction precisely showcase how dysregulated CSN6 pathways are integral to the progressive electrical and structural phenotypes found in ARVD/C patients with classic desmosomal mutations. More specifically, we also highlight the impact of the *DSP R315C* variant alone or in combination with other variants in predisposing the heart to ARVD/C disease susceptibility and progression. Thus, the strength of our data comes from the use of a multipronged approach that combines data from 5 different genetic mouse models (*Dsp*-cKO, *Csn6*-iKO, *Csn6*-cKO, Double Het, *Dsp* Hom mutant) and human cardiac biopsies/autopsies (harboring 6 distinct desmosomal mutations) alongside in silico data, which interrogate the CSN6-DSP interaction (in multiple ways) to provide evidence for a role for CSN6 in the mechanistic and pathological underpinnings of human ARVD/C.

The importance of maintaining desmosomal integrity is not only underscored in the human heart (resulting in ARVD/C), but also other organs, such as kidney (resulting in polycystic kidney disease) and skin (resulting in palmoplantar keratodermas), as well as a variety of cancers (gastric, colorectal, prostate, bladder, breast, skin, head/neck, cervical, endometrial) and autoimmune diseases (pemphigus foliaceus and pemphigus vulgaris) (4, 7). We anticipate that our findings will have broad implications toward highlighting master regulatory mechanisms that are inherent to the desmosome, which may have implications in understanding drivers of other desmosomal-based diseases, such as cancers in which desmosomal protein loss drives metastasis progression (4). Since neddylation inhibitors are in phase 1 clinical trials to treat metastatic melanoma, acute myeloid leukemia, and myelodysplastic syndromes (40, 41), our studies also provide disease indications and insights for subcellular targets of neddylation, which remain unclear in the field. Thus, our studies could also affect interpretations made from ongoing human clinical trials exploiting neddylation inhibitors as a therapeutic (40, 41).

Methods

Yeast-2-hybrid assays. Yeast-2-hybrid screens and forced yeast-2-hybrid assays were performed using the Matchmaker Gold Yeast Two-Hybrid System (Clontech). For the yeast-2-hybrid screen, N terminus DSP (1–519 amino acids) was cloned into pGBKT7 (bait plasmid) and transformed into the Y2HGold bait yeast strain (Clontech). Adult human heart cDNA library (Clontech Mate and Plate Library-Human Heart) served as prey and resided in a pGADT7 vector, which had been transformed into the Y187 yeast strain (Clontech). Mating and screening procedures were carried out as described by the manufacturer (Clontech). A very stringent cutoff for screening with fast growth on quadruple dropout plates was used for diploid yeast clones. After the screening, a total of 17 clones grew out. Colonies were further analyzed for active β-galactosidase using an X-gal filter lift assay. Plasmids from blue-positive clones were isolated and sequenced. Eleven different genes were identified using BLAST analysis, and 1 (strongest interaction) out of the 17 clones analyzed was *CSN6*. For forced yeast-2-hybrid assays, N terminus *DSP* (WT or *R315C*) and *PKP2* (WT) were cloned into pGBKT7 (bait plasmid) and transformed into

Y2HGold yeast strain (Clontech), while full-length CSN6 was cloned into pGADT7 (prey plasmid) and transformed into the Y187 yeast strain. Mating (pGBKT7 constructs with pGADT7 constructs) was carried out (Clontech) and interactions were assessed by β-galactosidase activity according to the manufacturer's instructions (Thermo Fisher). Negative controls (empty vector+CSN6; TD1+CSN6) and positive (p53+TD1) controls were used for β-galactosidase activity assays.

Molecular docking and mutational analysis. Structure information for human DSP (amino acids 179–625; RCSB Protein Data Bank [PDB] 3R6N) (16) and human CSN6 (chain N in RCSB PDB 4D10) (17) was uploaded to ClusPro2.0 (https://cluspro.bu.edu/) for molecular in silico docking (42, 43). No restraints were put on the protein-protein docking attempt. Resulting models should display a binding interface between the spectrin repeat encompassing R315 in DSP and the N-terminal MPN-domain in CSN6, as these were identified as minimal binding sites in our biochemical analyses. All models in the Van der Waals and electrostatic docking group matched these criteria. The model displaying the lowest energy score was further investigated (Figure 1B). For in silico modeling of the *R315C* mutation in *DSP*, structure minimization and calculation of energy changes (ΔΔG) was performed using YASARA and the FoldX module (44–46). The error margin of ΔΔG calculated by FoldX is approximately 0.5 kcal/mol, indicating that changes in that range are insignificant.

Experimental animals. Cardiac-specific *Dsp*-cKO mice have been previously generated and characterized (23). *Csn6* genomic DNA was isolated from the 129-SV/J mouse genomic DNA library (Stratagene). The *Csn6* conditional targeting vector was designed to include loxP sites, surrounding pGKNeo cassette, and exons 4–10 (Supplemental Figure 1A). G418-resistant embryonic stem (ES) cell clones were screened for homologous recombination by SpeI digestion, followed by Southern blot analysis, as previously described (47). A positive recombinant ES clone was microinjected into C57BL/6J blastocysts. Chimera mice were bred with C57BL/6J mice and crossed with *Sox2*-Cre mice (48) to selectively remove the pGKNeo cassette and generate *Csn6* floxed mice ($Csn6^{fl/fl}$). Cardiac-specific *Csn6* knockout mice (*Csn6*-cKO) were generated by crossing $Csn6^{fl/fl}$ mice with a-MHC-Cre, and cardiac inducible *Csn6* knockout mice (*Csn6*-iKO) were generated by crossing $Csn6^{fl/fl}$ mice with a-MHC-MerCreMer (Supplemental Figure 1B) (21, 22). Six-week-old *Csn6*-iKO mice and littermate controls were injected with tamoxifen (50 mg/kg/d) intraperitoneally once a day for 5 consecutive days (Supplemental Figure 1C).

Mouse lines harboring heterozygous *Dsp R315C* mutation (*Dsp R315C/+*) and heterozygous *Pkp2 IVS10-1 G>C* mutation (*Pkp2 IVS10-1 G>C/+*) were generated using CRISPR-Cas9–mediated methods that have been previously described (49). Briefly, CRISPR guide RNAs and single-strand oligodeoxynucleotide templates (ssODNs) were designed for *Dsp R315C* and *Pkp2 IVS10-1 G>C* mutations (Supplemental Table 1). CRISPR RNAs were chemically synthesized to contain the guide RNAs for *Dsp R315C* and *Pkp2 IVS10-1 G>C* mutations (Supplemental Table 1). For *Dsp R315C* mutant mice, a mixture of *Dsp R315C* cRNA, ssODNs, transactivating crRNA, and commercially available Cas9 protein was injected into pronuclei of 1-cell–stage zygotes from C57BL/6J mice (The Jackson Laboratory). For *Pkp2 IVS10-1 G>C* mutant mice, a mixture of *Pkp2 IVS10-1 G>C* cRNA, ssODNs, transactivating crRNA, and commercially available Cas9 protein was injected into pronuclei of 1-cell–stage zygotes from C57BL/6J mice (The Jackson Laboratory). Genomic DNA was extracted from mouse tails, and genomic fragments at target sites were amplified by PCR and sequencing. Genotype-positive knockin mice were backcrossed with C57BL/6J mice (The Jackson Laboratory) for at least 3 generations to minimize for potential off-target effects. Double-heterozygous (*Dsp R315C/+*; *Pkp2 IVS10-1 G>C/+*) mice were generated by crossing heterozygous *Dsp R315C* mutant mice with heterozygous *Pkp2 IVS10-1 G>C* mutant mice. *Dsp R315C* homozygous mutant mice were generated by crossing female heterozygous *Dsp R315C* mutant mice with male heterozygous *Dsp R315C* mutant mice.

Coimmunoprecipitation assays. Endogenous coimmunoprecipitation assays were performed as previously described (47). Adult mouse heart lysates were incubated overnight at 4°C with Protein G beads (GE Healthcare), which were preincubated with rabbit anti-CSN6 antibody (Enzolife, catalog BML-PW8295) or control rabbit IgG (MilliporeSigma, catalog I5006). Bound proteins were eluted, followed by SDS-PAGE and immunodetection of DSP (mouse, 1:1000, Bio-Rad, catalog 2722-5204), PKP2 (mouse, 1:1000, Fitzgerald, catalog 10R-P130b), and CSN6 (1:500, Enzolife, catalog BML-PW8295).

Protein analysis. Total and insoluble (intercalated disc-enriched) protein extracts were isolated from cardiomyocytes and ventricles, as previously described (23). Immunodetection of CSN6 (rabbit, 1:1000, Enzolife, catalog BML-PW8295), DSP (mouse, 1:1000, Bio-Rad, catalog 2722-5204), DSG2 (mouse, 1:300, Fitzgerald, catalog 10R-D106a), DSC2 (rabbit, 1:500, Fitzgerald, catalog 20R-DR004), PKP2 (mouse, 1:1000, Fitzgerald, catalog 10R-P130b), PKG (goat, 1:1000, MilliporeSigma, catalog SAB2500802), β-catenin (mouse, 1:1000, Cell Signaling Technology, catalog 8480), N-cadherin (rabbit, 1:1000, Abcam, catalog ab76057), connexin 43 (rabbit, 1:1000, Invitrogen, catalog 71-0700), talin2 (mouse, 1:1000, Bio-Rad, catalog MCA4771), vinculin (mouse, 1:1000, MilliporeSigma, catalog V9131), β_1-integrin (rabbit, 1:1000, gift from R.S. Ross, University of California San Diego), NEDD8 (rabbit, 1:1000, Cell Signaling Technology, catalog 2745), ubiquitin (rabbit, 1:1000, Cell Signaling Technology, catalog 3933), p62 (guinea pig, 1:1000, Progen Biotechnik GMBH, catalog 71001), glyceraldehyde 3-phosphate dehydrogenase (mouse, 1:2000, Santa Cruz Biotechnology Inc., catalog sc32233), cullin1 (rabbit, 1:1000, MilliporeSigma, catalog C7117), cullin2 (rabbit, 1:1000, Thermo Fisher, catalog 51-1800), cullin 3 (Mouse, 1:1000, Santa Cruz Biotechnology Inc., catalog sc-166053), cullin4A (rabbit, 1:1000, MilliporeSigma, catalog SAB1411512), cullin4B (rabbit, 1:1000, Abgent, catalog AP20232c), β-actin (mouse, 1:1000, Santa Cruz Biotechnology Inc., catalog sc47778), GST (mouse, 1:1000, Thermo Fisher, catalog MA4-004), and α-tubulin (mouse, 1:2000, MilliporeSigma, catalog T9028) was performed as previously described (23).

Immunofluorescence microscopy. Heart cryosections were fixed in 100% acetone at –20°C for 8 minutes and were blocked in 10% goat serum/PBS before incubation with antibodies. Human myocardial paraffin sections were deparaffinized, rehydrated, and heated for antigen retrieval, as previously described (50, 51). Sections were subsequently stained with primary antibodies against CSN6 (goat, 1:100, Santa Cruz Biotechnology Inc., catalog sc-47965 or rabbit, 1:100, Enzolife, catalog BML-PW8295), DSP (mouse, 1:1000, Bio-Rad, catalog 2722-5204), N-cadherin (rabbit, 1:100, Abcam, catalog ab76057), CSN5 (rabbit, 1:100, Cell Signaling Technology, catalog 6895S), PKG (goat, 1:100, MilliporeSigma, catalog SAB2500802), perilipin (rabbit, 1:100, Cell Signaling Technology, catalog 3470S), cullin 3 (mouse, 1:100, Santa Cruz Biotechnology Inc., catalog sc-166053), and sec-

ondary antibodies (1:100, Jackson ImmunoResearch Inc.). Immunofluorescence images were acquired using confocal microscopy (Olympus FV1000 or Leica SP8).

Electron microscopy. Cardiac ventricles were processed for electron microscopy, and images were captured with FEI Tecnai Spirit G2 BioTWIN Transmission Electron Microscope, as previously described (23).

RNA isolation and real-time PCR analyses. Total RNA was isolated from hearts using TRIzol (Invitrogen) according to the manufacturer's instructions. The first-strand cDNA was generated using PrimeScript RT Reagent Kit with gDNA Eraser (Takara). Real-time PCR was performed on heart cDNA using primer sequences (Supplemental Table 2) diluted in Power SYBR Green PCR Master Mix (Applied Biosystems) and using a Bio-Rad Mastercycler. All values were normalized to 18S and GAPDH mRNA levels.

Neonatal mouse ventricular cardiomyocyte isolation and treatments. Ventricular cardiomyocytes were isolated from neonatal (1 to 2 day old) mouse hearts and plated on laminin, as previously described (23). Cardiomyocytes were subsequently infected with adenoviruses harboring lacZ (MOI 100) and Cre (MOI 100) for 24 hours and then maintained in media consisting of DMEM, M199, 5% fetal bovine serum, 10% horse serum, and 1% penicillin/streptomycin/glutamine. For protein analyses, cardiomyocytes were collected at 4 days after infection. For CHX chase assays, *Csn6* floxed cardiomyocytes were infected with adenoviruses harboring lacZ (MOI 100) and Cre (MOI 100) for 48 hours, treated with CHX (10 μg/mL) for 0, 8, 16, 24, and 32 hours, and subjected to protein analysis. For CHX chase assays in Double Het cardiomyocytes, neonatal mouse cardiomyocytes isolated from Double Het and WT mice were treated with CHX (10 μg/mL) for 0, 8, 16, 24, 36, and 48 hours and subjected to protein analysis. For MLN4924 treatment studies, cardiomyocytes were treated with 1 μM MLN4924 or DMSO (vehicle) at 3 days after infection and collected for protein analyses 6 hours later.

Human myocardial tissues. Myocardial section was generated from a cardiac biopsy (formalin fixed, OCT embedded) from a patient harboring the *DSP R315C* and *PKP2 IVS10-1 G>C* mutation. This patient was referred to the Genetics of Cardiac Arrhythmia Program at the University of California San Francisco and fulfilled revised clinical and diagnostic task force criteria for definite ARVD/C (52) upon comprehensive evaluation by cardiac magnetic resonance imaging, echocardiography, electrophysiology study, and endomyocardial biopsy collection. Genetic testing on peripheral blood DNA was performed using a panel consisting of 7 known ARVD/C genes (PKP2, DSP, DSG2, DSC2, PKG, transmembrane protein 43, and ryanodine receptor-2) and using next-generation sequencing. Non-ARVD/C heart tissue used for Figure 5F was obtained from an explanted unused cadaveric donor heart at the time of organ donation, as the donor was not eligible for heart transplantation and the death was not cardiovascular related. Myocardial sections (formalin fixed, paraffin embedded) designated with mutations *DSP R1113X*, *DSP S1015fs1023X*, *DSP 1218+1G>A*, *PKP2 R413X*, and *PKP2 V570fs576X* were obtained from autopsied hearts from sudden deaths with diagnosis of ARVD/C with mutations identified in first-degree relatives and confirmed with genetic material from the deceased, as previously described (50, 51).

Histological analysis. Mouse hearts were perfused in a relaxation buffer consisting of 300 mM KCl in PBS and fixed with 4% paraformaldehyde. Fixed hearts were embedded in OCT Tissue-Tek (Sakura) or dehydrated and embedded in paraffin as previously described (23). Sections were cut between 5 and 10 μm thickness. Whole-heart (5 μM) paraffin sections were stained with H&E (Sigma-Aldrich) and Masson's trichrome (Sigma–Aldrich) stains according to the manufacturer's instructions. Whole-heart (10 μM) cryosections were stained with oil red O (Sigma–Aldrich) according to the manufacturer's instructions. Images were acquired with the Hamamatsu Nanozoomer 2.0 HT Slide Scanner.

MRI. In vivo cardiac MRI was performed on a 7T horizontal bore MR scanner (Bruker). A quadrature volume coil (Bruker) was used for RF signal transmission, and a 2-channel surface array coil (RAPID MRI) was used for reception of the RF signal. Cardiac CINE images were acquired with an IntraGate (Bruker) retrospective gated 2D gradient echo pulse sequence (FLASH) with the following parameters: TE = 3.1 ms, TR = 5.6 ms, flip angle = 7°, 300–400 repetitions, and 20 frames. A field of view equal to 2.0 cm × 1.5 cm and data matrix equal to 256 × 192 were prescribed for a spatial resolution equal to 0.078 mm/pixel. Equatorial frames containing the largest and smallest chamber diameters were selected to define the end-diastolic (ED) and end-systolic (ES) times, respectively. For MRI image analyses, 2D endocardial contours were manually segmented for each heart at ED and ES (LV and RV) using image analysis software (Seg3D, NIH Center for Integrative Biomedical Computing). Contour areas were calculated with custom software in MATLAB, multiplied by the slice spacing and summed together to approximate calibrated ED volumes (EDV) and ES volumes (ESV). Ejection fraction was defined as (EDV – ESV)/EDV × 100.

Echocardiography. Echocardiography was performed as previously described (47). Briefly, mice were anesthetized with 5% isoflurane for 15 seconds and maintained at 0.5% isoflurane during the procedure. The VisualSonics, SonoSite FUJIFILM, Vevo 2100 ultrasound system with a linear transducer 32–56MHz (MS550S) was used to capture the images and videos. Measurements of heart rate and percentage of FS as well as LV internal diameter at end-diastole (LVIDd) and end-systole (LVIDs) were determined from the M-mode tracing.

Surface and telemetry ECG. Surface ECG was performed as previously described (23). Briefly, mice were anesthetized with 5% isoflurane for 15 seconds and maintained at 1.5% isoflurane during the procedure. Six needle electrodes (30 gauge) were inserted subcutaneously into right forearm and left leg. For isoproterenol treatment studies, baseline surface ECG recordings were obtained in mice. Mice were subsequently injected intraperitoneally with isoproterenol (2.5 mg/kg body weight) and then reevaluated for surface ECG at 10 to 15 minutes after injection. For conscious telemetry studies, ECG transmitters (DSI) were subcutaneously inserted into the backs of mice as described previously (23). Positive and negative leads were fixed to the right shoulder muscle and the left leg muscle, respectively. ECG data was continuously acquired for 48 hours at 1 week after recovery from the implantation. ECG data were analyzed using LabChart. Quantification of ectopic beats within ECG tracings was calculated during a 5-minute interval every hour for a total of 5 hours.

Protein expression and GST pulldown assay. GST pulldown assay was performed as previously described (53). Briefly, full-length mouse *Csn6* was cloned into the pGEX-6P-1 vector (GE Life Sciences). GST-CSN6 and GST proteins were expressed in *E. coli* BL21 cells (Invitrogen; Life Technologies) and purified using Glutathione Sepharose 4B (GE Life Sciences). Protein concentration was determined through densitometry of Coomassie stained SDS-PAGE gels. Hearts were homogenized in lysis buffer (10 mM Tris-HCl pH 8.0, 100 mM NaCl, 0.2% Nonidet

P-40 and 1× protease and phosphatase inhibitors, 1 mM DTT). Heart extracts (500 μg per tube) were incubated with approximately 5 μg of GST or GST-CSN6 proteins on a rotator overnight at 4°C. Beads were washed 3 times with lysis buffer and resuspended in SDS-sample buffer. Bound proteins were analyzed through protein blot analyses.

Statistics. Data are presented in text and figures as mean values ± SEM. The sample size was defined by R software; α was set to 0.05 and power was 90% for all studies. GraphPad Prism was used for analyses, and significance was evaluated by Student's 2-tailed *t* test and 1-way or 2-way ANOVA following Tukey's or Šidák's multiple pairwise comparison tests. For Kaplan-Meier survival analysis, significance was assessed by the log-rank test. A *P* value of less than 0.05 was considered statistically significant.

Study approval. All animal procedures were approved by the University of California San Diego Animal Care and Use Committee. Procurement of ARVD/C human myocardial biopsy tissue was performed using standard procedures under protocols approved by the Institutional Ethics Review Board at the University of California San Francisco. Written, informed consent for biopsy procedures and use of explanted tissues prospectively was obtained.

Author contributions

FS conceived, designed,and supervised experiments. FS and YL wrote the manuscript. YL, RCL, TI, SL, and JB designed experiments. JP and RCL performed yeast-2-hybrid screen and forced yeast-2-hybrid analyses, respectively. TI and MHL generated and provided the *Csn6* targeting vector, respectively. RCL generated *Csn6* floxed mice and performed coimmunoprecipitation assays and immunofluorescence analyses on human ARVD/C heart tissue. YL generated cardiac-specific *Csn6*-KO mouse lines and performed molecular, histological, cellular, and ultrastructural studies as well as survival and electrophysiological analyses on *Csn6*-KO mouse lines as well as studies on *Dsp*-KO mice. SL and JB provided advice and performed molecular docking studies. KLP provided advice and supervised cardiac physiological studies. WHB and MB performed MRI and analyses of MRI images. NDD performed echocardiography analyses. YG performed telemetry studies. VN provided advice and use of non-ARVD/C heart tissue. MS and AA provided advice and use of heart tissue and genetics from ARVD/C patients.

Acknowledgments

We thank R.S. Ross (University of California San Diego) for providing β_1-integrin antibodies, W. Feng (University of California San Diego) for assistance with sgRNA design, and J. Blondelle (University of California San Diego) for technical assistance. We are grateful for support from the Neuroscience Microscopy Shared Facility and the Cellular and Molecular Medicine Electron microscopy core facility at the University of California San Diego. This work was supported by NIH National Heart Lung and Blood Institute grants HL142251 (to FS), HL128457 (to SL), HL095780 diversity supplement (to JP), and F31 predoctoral (HL120611) fellowship (to JP); California Institute of Regenerative Medicine grant RB3-05103 (to FS and MS); Tobacco Related Disease Research Program grant 24RT-022 (to FS); Department of Defense grant W81XWH1810380 (to FS); American Heart Association postdoctoral fellowships (to YL and RCL); and a National Science Foundation predoctoral fellowship (to WHB). The University of California San Diego Neuroscience Microscopy Shared Facility is supported by a grant from the NIH (P30 NS047101). The electron micrographs were taken in the Cellular and Molecular Medicine Electron microscopy core facility, which is supported in part by the NIH (award S10OD023527).

Address correspondence to: Farah Sheikh, Department of Medicine, University of California San Diego, 9500 Gilman Drive, La Jolla, California 92093, USA. Phone: 858.246.0754; Email address: fasheikh@health.ucsd.edu.

1. Su H, Wang X. The ubiquitin-proteasome system in cardiac proteinopathy: a quality control perspective. *Cardiovasc Res*. 2010;85(2):253–262.
2. Wang X, Robbins J. Proteasomal and lysosomal protein degradation and heart disease. *J Mol Cell Cardiol*. 2014;71:16–24.
3. Lyon RC, et al. Breaking down protein degradation mechanisms in cardiac muscle. *Trends Mol Med*. 2013;19(4):239–249.
4. Najor NA. Desmosomes in human disease. *Annu Rev Pathol*. 2018;13:51–70.
5. Sheikh F, et al. Cell-cell connection to cardiac disease. *Trends Cardiovasc Med*. 2009;19(6):182–190.
6. Vermij SH, et al. Refining the molecular organization of the cardiac intercalated disc. *Cardiovasc Res*. 2017;113(3):259–275.
7. Dusek RL, Attardi LD. Desmosomes: new perpetrators in tumour suppression. *Nat Rev Cancer*. 2011;11(5):317–323.
8. Delmar M, McKenna WJ. The cardiac desmosome and arrhythmogenic cardiomyopathies: from gene to disease. *Circ Res*. 2010;107(6):700–714.
9. Vimalanathan AK, et al. Genetics of and pathogenic mechanisms in arrhythmogenic right ventricular cardiomyopathy. *Biophys Rev*. 2018;10(4):973–982.
10. Nepomnyashchikh LM, et al. Focal degradation of cytoplasmic organelles in cardiomyocytes during regenerative and plastic myocardial insufficiency. *Bull Exp Biol Med*. 2000;130(12):1190–1195.
11. Lange S, et al. The kinase domain of titin controls muscle gene expression and protein turnover. *Science*. 2005;308(5728):1599–1603.
12. Hirschy A, et al. Stabilised beta-catenin in postnatal ventricular myocardium leads to dilated cardiomyopathy and premature death. *Basic Res Cardiol*. 2010;105(5):597–608.
13. Hilenski LL, et al. Immunolocalization of ubiquitin conjugates at Z-bands and intercalated discs of rat cardiomyocytes in vitro and in vivo. *J Histochem Cytochem*. 1992;40(7):1037–1042.
14. Balasubramanian S, et al. Enhanced ubiquitination of cytoskeletal proteins in pressure overloaded myocardium is accompanied by changes in specific E3 ligases. *J Mol Cell Cardiol*. 2006;41(4):669–679.
15. Kapplinger JD, et al. Distinguishing arrhythmogenic right ventricular cardiomyopathy/dysplasia-associated mutations from background genetic noise. *J Am Coll Cardiol*. 2011;57(23):2317–2327.
16. Choi HJ, Weis WI. Crystal structure of a rigid four-spectrin-repeat fragment of the human desmoplakin plakin domain. *J Mol Biol*. 2011;409(5):800–812.
17. Lingaraju GM, et al. Crystal structure of the human COP9 signalosome. *Nature*. 2014;512(7513):161–165.
18. Milic J, et al. Role of the COP9 signalosome (CSN) in cardiovascular diseases. *Biomolecules*. 2019;9(6):E217.
19. Wei N, et al. The COP9 signalosome: more than a protease. *Trends Biochem Sci*. 2008;33(12):592–600.
20. Su H, et al. Perturbation of cullin deneddylation via conditional Csn8 ablation impairs the ubiquitin-proteasome system and causes cardiomyocyte necrosis and dilated cardiomyopathy in mice. *Circ Res*. 2011;108(1):40–50.
21. Abel ED, et al. Cardiac hypertrophy with preserved contractile function after selective deletion of GLUT4 from the heart. *J Clin Invest*. 1999;104(12):1703–1714.
22. Sohal DS, et al. Temporally regulated and tissue-specific gene manipulations in the adult and

embryonic heart using a tamoxifen-inducible Cre protein. *Circ Res*. 2001;89(1):20–25.
23. Lyon RC, et al. Connexin defects underlie arrhythmogenic right ventricular cardiomyopathy in a novel mouse model. *Hum Mol Genet*. 2014;23(5):1134–1150.
24. Cavadini S, et al. Cullin-RING ubiquitin E3 ligase regulation by the COP9 signalosome. *Nature*. 2016;531(7596):598–603.
25. Birol M, et al. Structural and biochemical characterization of the Cop9 signalosome CSN5/CSN6 heterodimer. *PLoS One*. 2014;9(8):e105688.
26. Zhao Q, et al. Identification of rare variants of DSP gene in sudden unexplained nocturnal death syndrome in the southern Chinese Han population. *Int J Legal Med*. 2016;130(2):317–322.
27. Groeneweg JA, et al. Functional assessment of potential splice site variants in arrhythmogenic right ventricular dysplasia/cardiomyopathy. *Heart Rhythm*. 2014;11(11):2010–2017.
28. Svensson A, et al. Arrhythmogenic right ventricular cardiomyopathy — 4 Swedish families with an associated PKP2 c.2146-1G>C variant. *Am J Cardiovasc Dis*. 2016;6(2):55–65.
29. Thiene G, et al. Arrhythmogenic right ventricular cardiomyopathy/dysplasia. *Orphanet J Rare Dis*. 2007;2:45.
30. Sen-Chowdhry S, et al. Clinical and genetic characterization of families with arrhythmogenic right ventricular dysplasia/cardiomyopathy provides novel insights into patterns of disease expression. *Circulation*. 2007;115(13):1710–1720.
31. Quarta G, et al. Familial evaluation in arrhythmogenic right ventricular cardiomyopathy: impact of genetics and revised task force criteria. *Circulation*. 2011;123(23):2701–2709.
32. Denis A, et al. Arrhythmogenic response to isoproterenol testing vs. exercise testing in arrhythmogenic right ventricular cardiomyopathy patients. *Europace*. 2018;20(FI1):f30–f36.
33. Denis A, et al. Diagnostic value of isoproterenol testing in arrhythmogenic right ventricular cardiomyopathy. *Circ Arrhythm Electrophysiol*. 2014;7(4):590–597.
34. Cope GA, et al. Role of predicted metalloprotease motif of Jab1/Csn5 in cleavage of Nedd8 from Cul1. *Science*. 2002;298(5593):608–611.
35. Sharon M, et al. Symmetrical modularity of the COP9 signalosome complex suggests its multifunctionality. *Structure*. 2009;17(1):31–40.
36. Kotiguda GG, et al. The organization of a CSN5-containing subcomplex of the COP9 signalosome. *J Biol Chem*. 2012;287(50):42031–42041.
37. Su H, et al. The COP9 signalosome is required for autophagy, proteasome-mediated proteolysis, and cardiomyocyte survival in adult mice. *Circ Heart Fail*. 2013;6(5):1049–1057.
38. Kant S, et al. Histological and ultrastructural abnormalities in murine desmoglein 2-mutant hearts. *Cell Tissue Res*. 2012;348(2):249–259.
39. Te Rijdt WP, et al. Phospholamban p.Arg14del cardiomyopathy is characterized by phospholamban aggregates, aggresomes, and autophagic degradation. *Histopathology*. 2016;69(4):542–550.
40. Bhatia S, et al. A phase I study of the investigational NEDD8-activating enzyme inhibitor pevonedistat (TAK-924/MLN4924) in patients with metastatic melanoma. *Invest New Drugs*. 2016;34(4):439–449.
41. Swords RT, et al. Pevonedistat (MLN4924), a first-in-class NEDD8-activating enzyme inhibitor, in patients with acute myeloid leukaemia and myelodysplastic syndromes: a phase 1 study. *Br J Haematol*. 2015;169(4):534–543.
42. Comeau SR, et al. ClusPro: a fully automated algorithm for protein-protein docking. *Nucleic Acids Res*. 2004;32(Web Server issue):W96–W99.
43. Kozakov D, et al. The ClusPro web server for protein-protein docking. *Nat Protoc*. 2017;12(2):255–278.
44. Land H, Humble MS. YASARA: a tool to obtain structural guidance in biocatalytic investigations. *Methods Mol Biol*. 2018;1685:43–67.
45. Schymkowitz J, et al. The FoldX web server: an online force field. *Nucleic Acids Res*. 2005;33(web server issue):W382–W388.
46. Van Durme J, et al. A graphical interface for the FoldX forcefield. *Bioinformatics*. 2011;27(12):1711–1712.
47. Sheikh F, et al. An FHL1-containing complex within the cardiomyocyte sarcomere mediates hypertrophic biomechanical stress responses in mice. *J Clin Invest*. 2008;118(12):3870–3880.
48. Hayashi S, et al. Efficient gene modulation in mouse epiblast using a Sox2Cre transgenic mouse strain. *Gene Expr Patterns*. 2002;2(1–2):93–97.
49. Ma X, et al. CRISPR/Cas9-mediated gene manipulation to create single-amino-acid-substituted and floxed mice with a cloning-free method. *Sci Rep*. 2017;7:42244.
50. Asimaki A, et al. A new diagnostic test for arrhythmogenic right ventricular cardiomyopathy. *N Engl J Med*. 2009;360(11):1075–1084.
51. Syrris P, et al. Clinical expression of plakophilin-2 mutations in familial arrhythmogenic right ventricular cardiomyopathy. *Circulation*. 2006;113(3):356–364.
52. Marcus FI, et al. Diagnosis of arrhythmogenic right ventricular cardiomyopathy/dysplasia: proposed modification of the Task Force Criteria. *Eur Heart J*. 2010;31(7):806–814.
53. Lange S, et al. MLP and CARP are linked to chronic PKCα signalling in dilated cardiomyopathy. *Nat Commun*. 2016;7:12120.